Tunable photonic spin Hall effect in a tripod atom-light configuration

Muqaddar Abbas * and Pei Zhang †
Ministry of Education Key Laboratory for Nonequilibrium Synthesis and Modulation of Condensed Matter, Shaanxi Province Key Laboratory of Quantum Information and Quantum Optoelectronic Devices, School of Physics, Xi'an Jiaotong University, Xi'an 710049, China

Hamid R. Hamedi ‡
Institute of Theoretical Physics and Astronomy, Vilnius University, Saulėtekio 3, Vilnius LT-10257, Lithuania

(Received 8 December 2024; accepted 24 March 2025; published 7 April 2025)

We propose a four-level tripod atom-light coupling scheme to manipulate the photonic spin Hall effect (PSHE) in the reflected probe light. Our study demonstrates that the tripod configuration enables enhanced PSHE near the Brewster angle upon reflection for the probe field, with significantly stronger transverse shifts at resonance compared to off-resonance conditions. The PSHE shift is maximized when all fields are resonant, aligning with the transparency point of the system, and is notably weaker under off-resonant conditions, where gain effects dominate. Additionally, the tripod scheme enables an enhanced transverse shift for the signal field at resonance, resulting in dual-field PSHE enhancement. This combined enhancement of transverse shift for both probe and signal fields underscores the superiority of the tripod configuration in achieving maximized PSHE shifts, surpassing prior schemes and opening new possibilities for advanced applications in spin-photonic devices.

DOI: 10.1103/PhysRevA.111.043708

I. INTRODUCTION

Quantum coherence in multilayer atomic systems contributed to great theoretical as well as experimental interest owing to its capacity to significantly alter along with precisely regulate material optical characteristics. Laser-induced quantum coherence has a broad variety of applications in quantum optics, which gives birth to various intriguing phenomena, the most known of which is electromagnetically induced transparency (EIT) [1,2]. EIT is an optical method that uses the interference of electronic transitions in a material to reduce absorption along with substantially change dispersion across a small frequency range. Under typical conditions, resonant excitation leads to considerable absorption. However, when atoms are prepared using EIT, absorption is efficiently inhibited, contradicting the traditional relationship between a high refractive index with increased absorption [3].

EIT in its simplest form typically requires a three-level system. However, when a weak coherent electromagnetic field is introduced to a four-level EIT system, two simultaneous transparency windows are created—one for the probe field and another for the additional weak field—resulting in the so-called double EIT (DEIT) [4–8]. DEIT enhances the interaction duration between pulses due to reduced group velocities and enables the lossless propagation of two simultaneous signal fields [9]. These unique properties make DEIT a promising candidate for a variety of applications in quantum optics and quantum communication [10].

Schemes based on optical connections have garnered significant interest, particularly as the effective number of measured physical variables increases by orders of magnitude, leading to the observation of new physical phenomena and natural laws. One such phenomenon is the photonic spin Hall effect (PSHE), a cornerstone of spin photonics, which enables the spatial separation of light with opposite spin states in the transverse direction as a result of spin-orbit interactions of light [11,12]. This is distinct from the Goos-Hänchen (GH) shift [13–16], which describes the lateral displacement of a light beam from its expected geometrical trajectory. This effect is the optical analog of the spin Hall effect in electronic systems, where the refractive index gradient replaces the role of spin electrons and represents the equivalent of an electrical potential difference [17,18]. The PSHE was first predicted by Onoda *et al.* in 2004 [11] and was later expanded upon by Bliokh [12], who provided a comprehensive theoretical analysis. Empirical confirmation followed in 2008 when Hosten and Kwiat demonstrated the effect using weak measurement techniques [19].

The PSHE is now widely recognized as originating from the spin-orbit interaction of photons, consistent with the fundamental principle of angular momentum conservation in light [20,21]. Various mathematical and experimental methods have been developed to enhance PSHE, including weak value amplification, which significantly increases the transverse spin-dependent displacement linked to the Hall effect of the photonic spin [22,23]. While PSHE has been studied in a few atomic configurations [24–27], none of these schemes achieve simultaneous enhancement of PSHE in both

*Contact author: muqaddarabbas@xjtu.edu.cn
†Contact author: zhangpei@mail.ustc.edu.cn
‡Contact author: hamid.hamedi@tfai.vu.lt

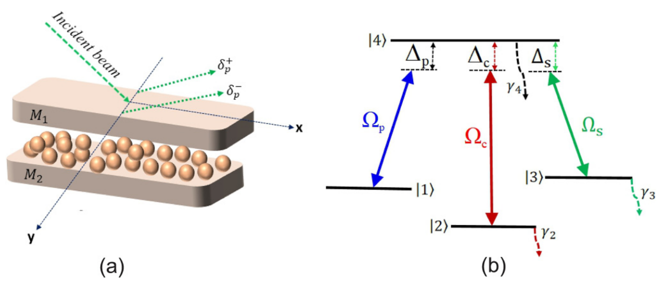

FIG. 1. (a) A three-layer cavity system with two mirrors, M_1 as well as M_2, along with coherent tripod atoms placed in between dielectric layers is shown schematically. (b) Energy level diagram of a four-level tripod atom-light coupling scheme interacting with two weak probe Ω_p and signal Ω_s beams, along with a stronger control field Ω_c.

probe and signal fields. Our proposed four-level tripod scheme uniquely enables dynamic and tunable dual-field PSHE enhancement, providing additional control and tunability that could be advantageous for practical applications.

The tripod scheme exhibits a variety of rich EIT phenomena, including what is referred to as double-DEIT (DDEIT) in Ref. [7]. The DDEIT phenomenon is characterized by the presence of two EIT windows for both the signal and probe fields under appropriate parameter conditions.

In this study, we investigate the four-level DDEIT tripod atomic system consisting of one upper state and three lower states. The system interacts with three simultaneous fields: a weak probe beam, a strong control beam, and a weak signal field. Using a semiclassical model, we analyze the tripod scheme to explore its interaction with the probe, control, and signal fields. The presence of double windows is observed for both the signal and probe fields, with EIT observed at resonance and gain emerging in another off-resonance window. Leveraging these features of probe and signal fields in tripod light-atom coupling, we examine the PSHE shift amplitude at resonance and off-resonance frequencies. The results show that the PSHE shift reaches its maximum at resonance due to EIT. Conversely, at off-resonance frequencies, the shift is suboptimal, likely influenced by gain effects present at those frequencies. Since similar behavior can be observed for the signal field, this implies a dual-field enhancement of the PSHE in the proposed tripod scheme.

II. THEORETICAL MODEL AND CALCULATION OF PHOTONIC SPIN HALL EFFECT

We analyze a probing light beam that is both TE and TM polarized, incoming from a vacuum at an angle of incidence θ_i on the cavity mirror M_1, as shown in Fig. 1(a). The monochromatic Gaussian probe beam may either transmit through the tripod atomic system or be reflected at its interface. The circular polarization components of the incident light beam on the right as well as on the left spatially separate upon reflection in a direction orthogonal to its plane of incidence (the y axis), as seen in Fig. 1(a). This spatial separation is referred to as the PSHE.

The PSHE is an optical phenomena that is reliant on polarization and results from the separation of photons with opposing helicities caused by the spin-orbit interaction of light. The transfer matrix approach is used to calculate the complex reflection coefficients for the TM-polarized R_M along with TE-polarized R_E components for the three-layer structure that is being addressed here. These coefficients can be expressed as:

$$R_{M,E} = \frac{\mathcal{R}_{M,E}^{12} + \mathcal{R}_{M,E}^{23}\exp(2ik_{2z}q)}{1 + \mathcal{R}_{M,E}^{12}\mathcal{R}_{M,E}^{23}\exp(2ik_{2z}q)}, \tag{1}$$

where q is the thickness of the intracavity medium, $\mathcal{R}_{M,E}^{12}$ and $\mathcal{R}_{M,E}^{23}$ are the reflection coefficients at the mirror one-intracavity tripod atom interface and the intracavity tripod atom-mirror two interface, respectively.

In the case of a two-layer reflection coefficient for the top mirror medium-lower mirror interface, the expression for the TM-polarized component is given by:

$$\mathcal{R}_M^{ij} = \frac{\epsilon_j k_{iz} - \epsilon_i k_{jz}}{\epsilon_j k_{iz} + \epsilon_i k_{jz}}, \tag{2}$$

and for TE polarized is

$$\mathcal{R}_E^{ij} = \frac{k_{iz} - k_{jz}}{k_{iz} + k_{jz}}. \tag{3}$$

Thus, $k_{iz} = \sqrt{k_0^2\epsilon_i - k_x^2}$ denotes the standard wave vector inside the respective layer, whereas $k_x = \sqrt{\epsilon_1}k_0\sin[\theta_i]$ represents the wave vector that moves in x direction. Additionally, $k_0 = 2\pi/\lambda$ represents a wave vector, having λ being the light wavelength.

Equation (1) shows that the reflection coefficients depend on the permittivity of the cavity walls, ϵ_1 and ϵ_3, which remain constant, as well as the permittivity of the intracavity medium, ϵ_2. The latter corresponds to the tripod atomic medium and can be actively controlled by modifying the susceptibility χ_p. The relationship between the permittivity of the intracavity medium and the susceptibility of the tripod atomic system is given by:

$$\epsilon_2 = 1 + \chi_p, \tag{4}$$

where χ_p represents the susceptibility of the tripod atomic system, which can be calculated using the density matrix formalism described in Sec. III. This tunability enables dynamic control over the PSHE of light.

For a TM-polarized Gaussian beam that is reflected by the interface between surfaces, the field-effect amplitudes for the two circular components of reflected light are ordered in the following manner within the reflection systems:

$$\mathcal{E}_r^{\pm}(x_r, y_r, z_r) = \frac{\omega_0}{\omega}\exp\left[-\frac{x_r^2 + y_r^2}{\omega}\right] \times \left[R_M - \frac{2ix_r}{k\omega}\frac{\partial R_M}{\partial\theta} \mp \frac{2y_r\cot[\theta]}{k\omega} \times (R_E + R_M)\right], \tag{5}$$

where $\omega = \omega_0[1 + (2z_r/k_1\omega_0^2)^2]^{1/2}$, $z_r = k_1\omega_0^2/2$ is the Rayleigh length, the incident beam's waist radius ω_0, (x_r, y_r, z_r) displays the coordinate system for reflected light and the superscript $\pm$ denotes the various spin states.

Then, the transverse displacement of reflected light can be expressed as

$$\delta_p^{\pm} = \frac{\int y|\mathcal{E}_r^{\pm}(x_r, y_r, z_r)|^2 dx_r dy_r}{\int |\mathcal{E}_r^{\pm}(x_r, y_r, z_r)|^2 dx_r dy_r}. \tag{6}$$

Based on Eq. (5) as well as Eq. (6), the transverse spin-displacement components δ_p^+ along with δ_p^- may be articulated to the refractive coefficients of the three-layer cavity tripod system's represented as [28,29]

$$\delta_p^{\pm} = \mp \frac{k_1\omega_0^2 \mathrm{Re}\left[1+\frac{R_E}{R_M}\right]\cot\theta_i}{k_1^2\omega_0^2 + \left|\frac{\partial lnR_E}{\partial\theta_i}\right|^2 + \left|\left(1+\frac{R_E}{R_M}\right)\cot\theta_i\right|^2}. \tag{7}$$

Here $\delta_p^{\pm}$ denotes the transverse shift between the left and right circularly polarized components of the incident light with $k_1 = \sqrt{\epsilon_1}k$. In what follows, we will concentrate on the transverse shift δ_p^+ of the left circularly polarized component. Since the two spin components have equal magnitudes but opposite directions, the shift of the right circularly polarized component can be adjusted concurrently.

III. INTRACAVITY TRIPOD ATOMIC SYSTEM

Figure 1(b) displays a tripod system's detailed schematic. The probing, control, along with signal beams, correspondingly, connect three ground states to an excited state in a tripod system. The transition $|1\rangle \leftrightarrow |4\rangle$ is subjected to the weaker probing laser Ω_p. The control as well as signal beams couple to generate atomic transition $|2\rangle \leftrightarrow |4\rangle$ along with $|3\rangle \leftrightarrow |4\rangle$, respectively, having Rabi frequencies Ω_c as well Ω_s. The detunings of the probe, control, as well as signal fields are indicated by the parameters Δ_p, Δ_c, and Δ_s. For $j \in \{2, 3, 4\}$, the decay rates of the levels $|j\rangle$ are represented by γ_j.

Taking into account the rotating wave along with dipole approximations, the semiclassical Hamiltonian that describes the tripod-type atomic system is [7]

$$\begin{aligned}\hat{H}' &= \Delta_\mathrm{pc}\hat{\sigma}_{22} + \Delta_\mathrm{ps}\hat{\sigma}_{33} + \Delta_\mathrm{p}\hat{\sigma}_{44} \\ &\quad + \frac{\hbar}{2}(\Omega_\mathrm{p}\hat{\sigma}_{14} + \Omega_\mathrm{c}\hat{\sigma}_{24} + \Omega_\mathrm{s}\hat{\sigma}_{34} + \mathrm{H.c.}),\end{aligned} \tag{8}$$

wherein $\Delta_\mathrm{xy} := \Delta_\mathrm{x} - \Delta_\mathrm{y}$ denotes the two-photon detuning, whereas H.c. denotes the Hermitian conjugate. The evolution of time in the quantum master equation may be used to calculate the tripod atom-light coupling response relative to the applied fields [7]

$$\begin{aligned}\dot{\rho} &:= -\frac{i}{2}[\rho, \hat{H}'] + \sum_{i<j}^{4} \frac{\gamma_{ji}}{2}(\sigma_{ij}\rho\sigma_{ji} - \sigma_{jj}\rho - \rho\sigma_{jj}) \\ &\quad + \sum_{j=1}^{4} \frac{\gamma_{\phi j}}{2}(\sigma_{jj}\rho\sigma_{jj} - \sigma_{jj}\rho - \rho\sigma_{jj}).\end{aligned} \tag{9}$$

Both spontaneous emissions as well as dephasing are included in Eq. (9). Here, the rate at which decay occurs between the states $|j\rangle \rightarrow |i\rangle$ is represented by γ_{ji}, whereas the dephasing rate of the state $|j\rangle$ is indicated by $\gamma_{\phi j}$. The complete set of equations for the density matrix ρ can be found in Ref. [30].

We now turn to Eq. (9) to derive the equation for the off-diagonal element ρ_{14} of the density matrix in the steady-state regime, which describes the interaction with the probe light. The optical response to the probe field can be expressed in terms of the off-diagonal steady-state density-matrix element ρ_{14}, as follows:

$$\rho_{14} = \Omega_\mathrm{p}\frac{i(\rho_{11} - \rho_{44}) + \frac{\Omega_\mathrm{s}}{\gamma_3 - 2i\Delta_\mathrm{ps}}\rho_{43}}{\gamma_4 - 2i\Delta_\mathrm{p} + \frac{|\Omega_\mathrm{c}|^2}{\gamma_2 - 2i\Delta_\mathrm{pc}} + \frac{|\Omega_\mathrm{s}|^2}{\gamma_3 - 2i\Delta_\mathrm{ps}}}, \tag{10}$$

where

$$\rho_{43} = \Omega_\mathrm{s}^*\frac{-i(\rho_{33} - \rho_{44}) + \frac{\Omega_\mathrm{p}^*}{\gamma_3 - 2i\Delta_\mathrm{ps}}\rho_{14}}{\Gamma_{43} + 2i\Delta_\mathrm{s} + \frac{|\Omega_\mathrm{c}|^2}{\Gamma_{32} + 2i\Delta_\mathrm{sc}}}, \tag{11}$$

with $\Gamma_{kl} = \gamma_k + \gamma_l$. The electric susceptibility of the system for the probe field χ_p characterizing the absorption and dispersion properties of the weak probe field is defined by

$$\chi_\mathrm{p} = \eta_\mathrm{p}\frac{\rho_{14}}{\Omega_\mathrm{p}}, \quad \eta_\mathrm{p} = \frac{\mathcal{N}|\boldsymbol{\mu}_{14}|^2}{\epsilon_0\hbar}, \tag{12}$$

where in Eq. (12) $\mathcal{N}$, $\boldsymbol{\mu}_{14}$, ϵ_0 and $\hbar$ represent the atomic number density, dipole moments, permittivity of the free space, and Planck constant, respectively. The final probe susceptibility equation then using Eqs. (10)–(12) is

$$\chi_\mathrm{p} = i\eta_\mathrm{p}\frac{(\rho_{11} - \rho_{44})\left(\Gamma_{43} + 2i\Delta_\mathrm{s} + \frac{|\Omega_\mathrm{c}|^2}{\Gamma_{32} + 2i\Delta_\mathrm{sc}}\right) + (\rho_{11} - \rho_{44})\frac{|\Omega_\mathrm{p}|^2}{\gamma_3 - 2i\Delta_\mathrm{ps}} + (\rho_{44} - \rho_{33})\frac{|\Omega_\mathrm{s}|^2}{\gamma_3 - 2i\Delta_\mathrm{ps}}}{\left(\Gamma_{43} + 2i\Delta_\mathrm{s} + \frac{|\Omega_\mathrm{c}|^2}{\Gamma_{32} + 2i\Delta_\mathrm{sc}}\right)\left(\gamma_4 - 2i\Delta_\mathrm{p} + \frac{|\Omega_\mathrm{c}|^2}{\gamma_2 - 2i\Delta_\mathrm{pc}} + \frac{|\Omega_\mathrm{s}|^2}{\gamma_3 - 2i\Delta_\mathrm{ps}}\right) + \frac{|\Omega_\mathrm{p}|^2}{\gamma_3 - 2i\Delta_\mathrm{ps}}\left(\gamma_4 - 2i\Delta_\mathrm{p} + \frac{|\Omega_\mathrm{c}|^2}{\gamma_2 - 2i\Delta_\mathrm{pc}}\right)}. \tag{13}$$

A similar approach can be applied to the case of the signal field, yielding an analogous equation for the signal beam susceptibility.

IV. PSHE FOR TRIPOD SYSTEM

In this section, we present the results for the PSHE, focusing on the scenario where the control field is resonant, while the signal field remains off resonant. The population is assumed to be distributed between states $|1\rangle$ and $|3\rangle$. This configuration leads to the EIT at the resonant frequency and gain at the off-resonant window of the probe field. We use experimentally feasible parameters to elucidate the underlying mechanisms of this scheme, incorporating the theoretical framework of the PSHE.

In Fig. 2(a), we show the response of the tripod atomic system to the probe field when the signal field is off resonant and the detuning of the strong control field is set to zero. In this configuration, we observe the emergence of two distinct windows. The first window appears when the detunings of all

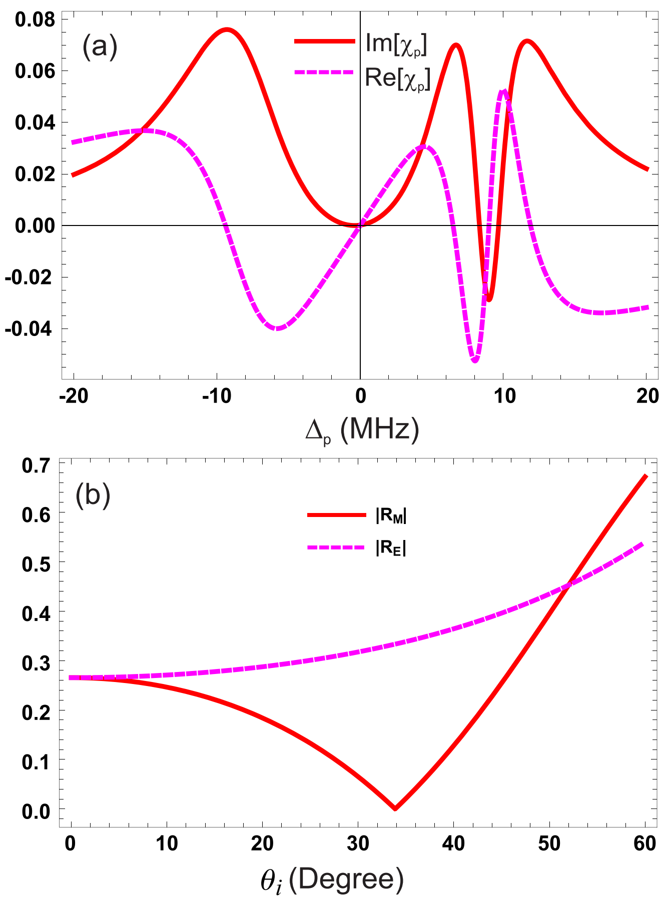

FIG. 2. (a) The graphical representation of Im[χ] (pink solid line) along with Re[χ] (red dashed line) against the probe detuning Δ_p using Eq. (13). (b) Absolute values $|R_E|$ and $|R_M|$ versus incidence angle θ_i for $\Delta_p = 0$. The other parameters are $\Delta_s = 9$ MHz, $\Delta_c = 0$, $\Omega_c = 1\gamma_4$, $\Omega_s = 0.3\gamma_4$, $\Omega_p = 0.2\gamma_4$, $\mathcal{N} = 10^{14}$ cm^{-3}, $\boldsymbol{\mu}_{14} = 1.269 \times 10^{-29}$ Cm, $\Gamma_{43} = 18.01$ MHz, $\gamma_4 = 18$ MHz, $\gamma_2 = 40$ kHz, $\gamma_3 = 10$ kHz. The additional parameters for plotting $|R_E|$ and $|R_M|$ are $\epsilon_1 = \epsilon_2 = 2.22$, $\lambda = 852$ nm, and thickness of intracavity medium $q = 100$ nm.

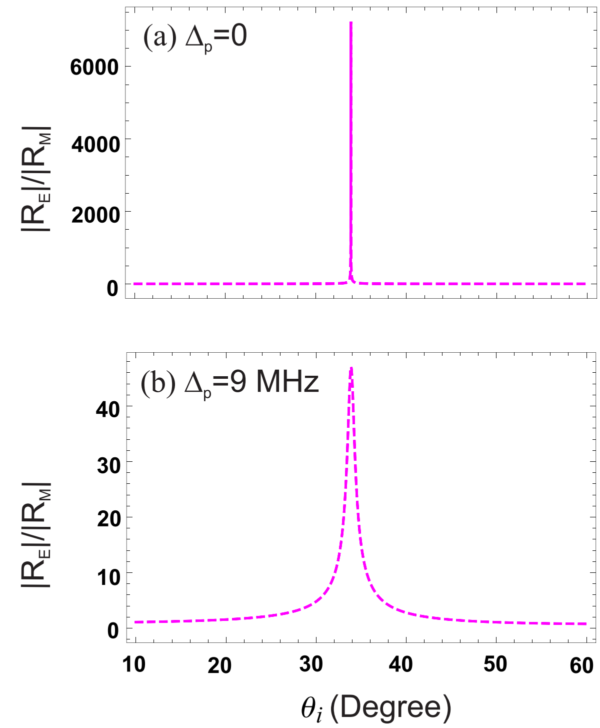

FIG. 3. Ratio $|R_E/R_M|$ of reflection coefficient versus incidence angle θ_i for (a) $\Delta_p = 0$ and (b) $\Delta_p = 9$ MHz. The other parameters are $\Delta_s = 9$ MHz, $\Delta_c = 0$, $\Omega_c = 1\gamma_4$, $\Omega_s = 0.3\gamma_4$, $\Omega_p = 0.2\gamma_4$, $\mathcal{N} = 10^{14}$ cm^{-3}, $\boldsymbol{\mu}_{14} = 1.269 \times 10^{-29}$ Cm, $\Gamma_{43} = 18.01$ MHz, $\gamma_4 = 18$ MHz, $\gamma_2 = 40$ kHz, $\gamma_3 = 10$ kHz, $\epsilon_1 = \epsilon_2 = 2.22$, $\lambda = 852$ nm, and thickness of intracavity medium $q = 100$ nm.

applied fields are equal, meaning they are all in resonance, which results from destructive interference between the indirect channels [31]. The second window occurs when the detunings of the probe and signal fields are the same and set to 9 MHz, while the detuning of the control field is zero. The second window is narrow and is characterized by negative absorption or amplification, a phenomenon caused by the Raman gain effect.

This observed gain can be attributed to signal-induced coherence, as described by Eq. (10). The gain involves two contributions: one associated with the population difference $\rho_{11} - \rho_{44}$ and the other with ρ_{43} [7]. Gain is shown when $\Delta_p = \Delta_s$, where the first term's imaginary part is positive while the second term's imaginary part is negative. Through the $|1\rangle \leftrightarrow |3\rangle$ transition, the probe gain is caused by signal-driven coherence, proving that this coherence connects the transitions generated by the signal along with probe fields.

It is clear from Eq. (7) that the reflection coefficients for TE- along with TM-polarized input light have a significant impact on the transverse shift $\delta_p^{\pm}/\lambda$. To investigate this further, we analyze how these reflection coefficients vary with the angle of incidence. Figure 2(b) displays the magnitudes of the reflection coefficients for TE-polarized light, R_E, and TM-polarized light, R_M. As illustrated in Fig. 2(b), the TM-polarized reflection coefficient R_M (represented by the red solid curve) initially decreases as the incident angle increases, reaching zero at the Brewster angle $\theta_B \approx 34^\circ$. Beyond this point, R_M increases again as the angle of incidence continues to rise. In contrast, the TE-polarized reflection coefficient R_E (depicted by the pink dashed curve) shows a steady increase with increasing incident angle. This contrasting behavior of R_M and R_E with respect to the angle of incidence underscores the angle-dependent nature of the light's interaction with the surface.

According to Eq. (7), the transverse shift $\delta_p^{\pm}/\lambda$ is determined by the ratio of the TE- and TM-polarized reflection coefficients, R_E and R_M, at a specific angle of incidence. A pronounced transverse shift emerges when this ratio exceeds unity. To investigate this relationship further, we analyze the ratio $|R_E/R_M|$ as a function of the incident angle θ_i, for both the resonant condition ($\Delta_p = 0$) and the off-resonant condition ($\Delta_p = 9$ MHz), depicted in Fig. 3. The most prominent observation from Fig. 3 is that the ratio $|R_E/R_M|$ reaches its maximum under resonance ($\Delta_p = 0$), surpassing the values observed in the off-resonant region. Additionally, the ratio experiences a steep rise near the Brewster angle, $\theta_B \approx 34^\circ$, in both cases. As illustrated by the red curve in Fig. 2(b),

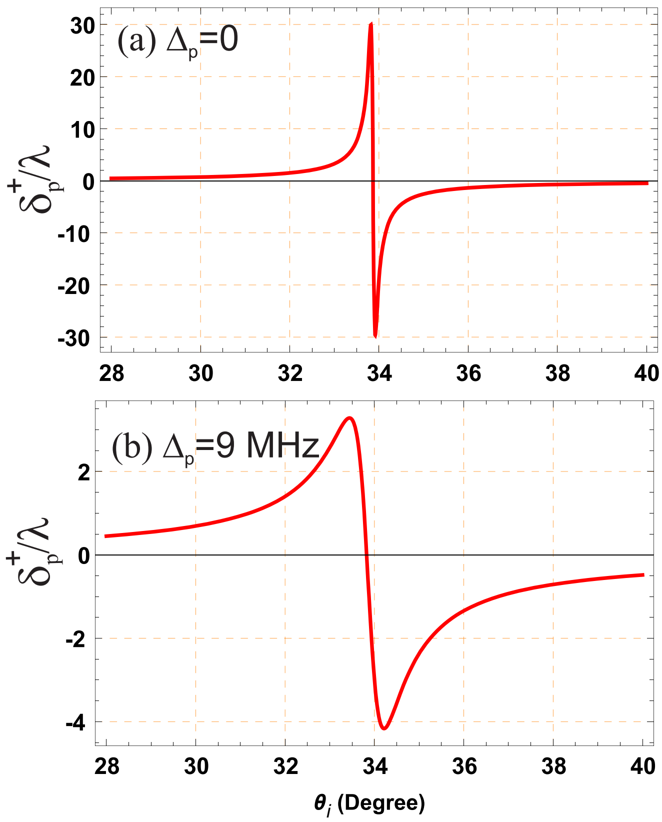

FIG. 4. The PSHE shift δ_p^+/λ versus incidence angle θ_i for (a) $\Delta_p = 0$ and (b) $\Delta_p = 9$ MHz. The other parameters are $\Delta_s = 9$ MHz, $\Delta_c = 0$, $\Omega_c = 1\gamma_4$, $\Omega_s = 0.3\gamma_4$, $\Omega_p = 0.2\gamma_4$, $\mathcal{N} = 10^{14}$ cm^{-3}, $\boldsymbol{\mu}_{14} = 1.269 \times 10^{-29}$ Cm, $\Gamma_{43} = 18.01$ MHz, $\gamma_4 = 18$ MHz, $\gamma_2 = 40$ kHz, $\gamma_3 = 10$ kHz, $\epsilon_1 = \epsilon_2 = 2.22$, $\lambda = 852$ nm, $q = 100$ nm and beam waist $\omega_0 = 60\lambda$.

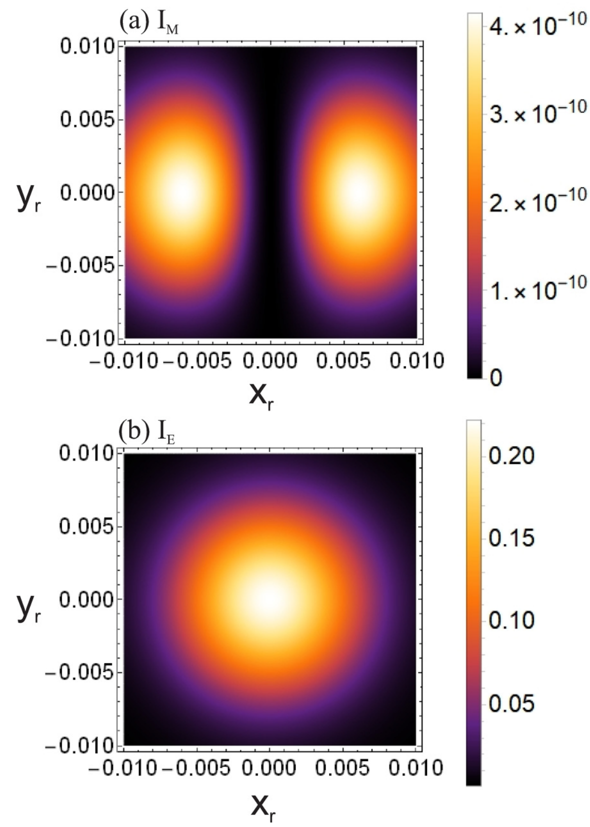

FIG. 5. The distribution of the electric field intensity for (a) transverse magnetic (TM, p-polarized) and (b) transverse electric (TE, s-polarized) waves as a function of the spatial coordinates x_r and y_r in the reflection plane, analyzed near the Brewster angle θ_B. The other parameters are $\Delta_s = 9$ MHz, $\Delta_c = 0$, $\Omega_c = 1\gamma_4$, $\Omega_s = 0.3\gamma_4$, $\Omega_p = 0.2\gamma_4$, $\mathcal{N} = 10^{14}$ cm^{-3}, $\boldsymbol{\mu}_{14} = 1.269 \times 10^{-29}$ Cm, $\Gamma_{43} = 18.01$ MHz, $\gamma_4 = 18$ MHz, $\gamma_2 = 40$ kHz, $\gamma_3 = 10$ kHz, $\epsilon_1 = \epsilon_2 = 2.22$, $\lambda = 852$ nm, $q = 100$ nm and beam waist $\omega_0 = 60\lambda$.

the reflection coefficient $|R_M|$ diminishes to nearly zero at the Brewster angle, leading to a sharp increase in $|R_E/R_M|$. This near vanishing of $|R_M|$ significantly amplifies the ratio. To capture the influence around the Brewster angle accurately, we limit our analysis to a narrow interval of incident angles θ_i.

We now turn our attention to the transverse shift induced by the PSHE. For the sake of simplicity and clarity, we focus specifically on the transverse shift associated with the right circularly polarized photon spin-dependent component, which we denote as δ_p^+/λ. This focus is motivated by the fact that, for the two circular polarization states, the transverse shifts are equal in magnitude but opposite in direction. This symmetry allows us to concentrate on one polarization component while understanding that the behavior of the left circularly polarized component will mirror that of the right one, but with a reversed direction of the shift.

We analyze the PSHE, δ_p^+/λ, as a function of the incident angle θ_i, comparing two specific regimes: the resonant condition at $\Delta_p = 0$, where transparency is observed [Fig. 4(a)], and the off-resonant case at $\Delta_p = 9$ MHz, characterized by gain [Fig. 4(b)]. To ensure a clear and meaningful comparison, we maintain consistent parameters across both scenarios. Our results reveal a pronounced enhancement of the PSHE under resonant conditions compared to the off-resonant case. This enhancement can be attributed to the EIT and the transparency window that occurs at resonance, in contrast to the gain-induced amplification present in the off-resonant scenario.

Next, we present a numerical simulation of the reflected electric field intensity distribution for TM polarization, defined as $I_M = |\mathcal{E}_r^+ + \mathcal{E}_r^-|^2$, as a function of the spatial coordinates x_r and y_r. This distribution is analyzed near the Brewster angle, where partial reflection of the incident beam occurs. The resulting intensity profile, shown in Fig. 5(a), reveals two high-intensity spots symmetrically positioned on either side of $x_r = 0$, separated by a central dark region. This dark region corresponds to suppressed TM reflection at the Brewster angle ($R_M \to 0$), while the two lobes arise from spin-orbit coupling (SOC)-induced longitudinal phase gradients ($\propto \frac{\partial R_M}{\partial \theta}$) in Eq. (5). These phase gradients reshape the Gaussian beam into two lobes via constructive or destructive interference between the reflected spin components ($\mathcal{E}_r^+$ and $\mathcal{E}_r^-$). While the transverse PSHE shift originates from spin-dependent displacements $\propto \pm\frac{2\cot\theta}{k\omega}(R_E + R_M)$, these shifts cancel out in the total intensity $I_M = |\mathcal{E}_r^+ + \mathcal{E}_r^-|^2$, as $\mathcal{E}_r^+$ and $\mathcal{E}_r^-$ experience equal and opposite displacements along y_r.

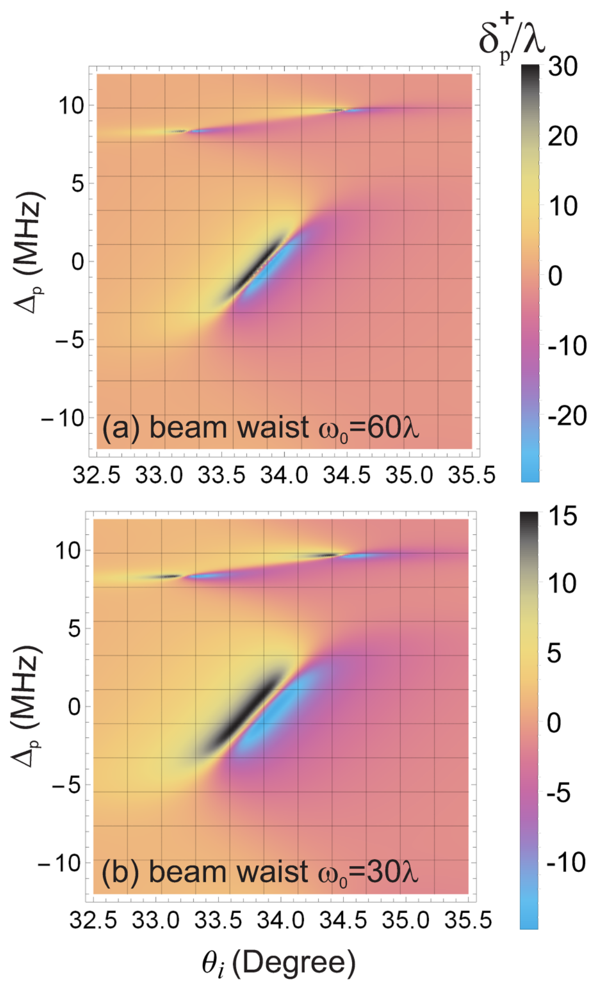

FIG. 6. Density plot of PSHE shift δ_p^+/λ versus probe field detuning Δ_p and incidence angle θ_i for (a) beam waist $\omega_0 = 60\lambda$ and (b) beam waist $\omega_0 = 30\lambda$. The other parameters are $\Delta_c = 0$, $\Omega_c = 1\gamma_4$, $\Omega_s = 0.3\gamma_4$, $\Omega_p = 0.2\gamma_4$, $\mathcal{N} = 10^{14}$ cm^{-3}, $\boldsymbol{\mu}_{14} = 1.269 \times 10^{-29}$ Cm, $\Gamma_{43} = 18.01$ MHz, $\gamma_4 = 18$ MHz, $\gamma_2 = 40$ kHz, $\gamma_3 = 10$ kHz, $\epsilon_1 = \epsilon_2 = 2.22$, $\lambda = 852$ nm, and $q = 100$ nm.

Consequently, no net transverse shift is observed in I_M. The true PSHE shift is instead explicitly quantified in Fig. 3 (through the ratio $|R_E/R_M|$) and Fig. 4.

Similarly, Fig. 5(b) presents the electric field intensity distribution for TE polarization, given by $I_E = |\mathcal{E}_e^+ + \mathcal{E}_e^-|^2$, as a function of x_r and y_r near the Brewster angle. While $E_e^\pm$ is not explicitly defined in the paper, replacing the TM reflection coefficient R_M with the TE reflection coefficient R_E in Eq. (5) provides the necessary relation [29]. Unlike TM polarization, TE lacks Brewster-angle suppression ($R_E \neq 0$) and SOC effects are significantly weaker ($\partial R_E/\partial\theta \ll \partial R_M/\partial\theta$). As a result, the TE intensity distribution exhibits a symmetric Gaussian profile. This confirms that transverse shifts in reflected beams are far more pronounced in TM polarization.

Figure 6 presents a density plot of the PSHE as a function of the incident angle θ_i and probe field detuning Δ_p for varying beam waists (ω_0) of the incident beam. From Fig. 6(a), it is evident that the PSHE reaches its maximum when the beam waist is $\omega_0 = 60\lambda$. For larger beam waists, the beam becomes less tightly focused, resulting in a broader spatial distribution of the light intensity. This broader distribution allows for a more gradual change in the polarization state across the beam profile, which enhances the spatial separation of photons with different helicities. Consequently, the PSHE is more pronounced. In contrast, when the beam waist is reduced to $\omega_0 = 30\lambda$, the PSHE magnitude diminishes, see Fig. 6(b). The smaller beam waist confines the light field more tightly, leading to sharper polarization gradients and less effective separation of helicities. This confinement reduces the spatial extent over which the polarization changes, thereby limiting the spin Hall effect.

Similar to the behavior observed for the probe field, the PSHE can also be expected for the signal field (which is not shown here). A double-window structure would emerge: an EIT window when the signal field is resonant ($\Delta_s = 0$) and a gain window in the nonresonant condition ($\Delta_s = \Delta_p = 9$ MHz). A significant enhancement of the PSHE is expected for the signal field in the resonant case ($\Delta_s = 0$), corresponding to the EIT condition, while a comparatively weaker transverse shift would be observed in the nonresonant case ($\Delta_s = \Delta_p = 9$ MHz), corresponding to gain.

This behavior suggests that, in addition to the initial enhancement of the PSHE for the probe field at its resonance, a similarly pronounced enhancement could also occur for the signal field when $\Delta_s = 0$. This potential dual-field PSHE enhancement highlights the versatility along with potential applications of the system in tunable and amplified spin-photon interactions, offering a significant advantage by achieving strong resonance transverse shifts in both channels. Compared to previous scenarios [24–26], which enable controllable PSHE for only a single weak field, this approach opens new possibilities for applications in spin-related technologies.

This dual-field PSHE configuration offers a significant advantage by achieving stronger transverse shifts at resonance in both channels compared to the off-resonance condition. This enhancement is driven by nonlinear interactions in the system, which amplify spin-photon coupling and enable precise manipulation of light's spin and polarization. Such control is crucial for applications in quantum communication, optical spintronics, and advanced optical communication systems. The sensitivity of the nonlinear configuration to resonance conditions allows for sharper and more tunable effects, ideal for high-precision applications such as optical switching and sensing. Moreover, the enhanced EIT-induced interactions improve the efficiency of devices such as sensors and quantum memory systems, while opening new possibilities for innovative technologies in quantum optics and metrology.

This study focuses on the fundamental mechanisms underlying PSHE shifts while considering practical factors such as Doppler broadening, atom-surface interactions, and collisional broadening. While a full theoretical treatment of these effects is beyond the scope of this work, our predictions are most relevant to setups where Doppler broadening is minimized. Ultrathin vapor cells and cold-atom systems, where atomic motion is confined or laser cooling suppresses velocity-dependent broadening, provide promising experimental platforms. Our calculations, based on the density matrix formalism, neglect Doppler broadening to isolate the intrinsic medium response. In practice, magneto-optical traps effectively eliminate Doppler effects, while counterpropagating beam techniques have been shown to reduce broadening in warm atomic vapors [32]. Atom-surface interactions in cavity-based cold-atom experiments, including van der Waals and Casimir-Polder forces, can induce spectral broadening. However, precise optical trapping can mitigate these effects by controlling atom-surface distances. Additionally, alternative platforms such as nanophotonic waveguides and optomechanical cavities naturally restrict atomic motion, reducing broadening effects.

V. CONCLUDING REMARKS

In this work, we presented a theoretical investigation of enhancing the PSHE in reflected probe light within a tripod atomic system. Using the transfer matrix approach, we calculated the reflection coefficients for TE and TM modes, highlighting a high ratio of these coefficients that demonstrates PSHE amplification. A pronounced peak in the transverse shift was observed around the Brewster angle. We have shown that the magnitude of the transverse shift can be effectively tuned by varying the resonance conditions. Specifically, the PSHE shift amplitude is higher at resonance ($\Delta_p = 0$), corresponding to the EIT condition, and significantly reduced at off resonance ($\Delta_p = 9\gamma$), where gain effects dominate. Additionally, we found that the PSHE becomes more pronounced with a larger beam waist, resulting in a stronger transverse shift compared to smaller beam waists. This behavior emphasizes the role of beam geometry in controlling the effect. Similar to the behavior observed for the probe field, the PSHE is also evident for the signal field, meaning that the tripod scheme allows for achieving dual-channel enhancement of PSHE for both probe and signal fields at the resonance condition. This offers a significant advantage due to its stronger and more controllable PSHE response, driven by the nonlinear interactions present in the system.

Unlike previous studies that focused on a single weak field, the tripod scheme naturally enables simultaneous enhancement of the transverse shifts for both the probe and signal fields at resonance. This dual-field response emerges from the coherent interactions within the system, allowing for a more tunable and controllable PSHE. The ability to enhance and manipulate spin-dependent shifts in both channels provides a broader parameter space for optimizing PSHE effects compared to conventional schemes. Furthermore, the flexibility in adjusting resonance conditions and beam parameters in this system makes it well suited for applications in spin-photonic devices and quantum optical technologies, where precise control over light-matter interactions is essential.

To justify the parameter selection in our simulations, we refer to Fig. 1(b). In particular, we analyze the atomic structure of ^{87}Rb, where the states $|1\rangle$, $|2\rangle$, and $|3\rangle$ correspond to the $5S_{1/2}$ manifold, with quantum numbers $F = 1, m_F = 0$ and $F = 2, m_F = \{-2, 0\}$, respectively. Additionally, state $|4\rangle$ is associated with the $5P_{1/2}$ level, specifically $F = 2$ and $m_F = -1$ [6]. The decay rates and field strengths incorporated into the simulations, assuming an atomic density of 10^{14} cm^{-3}, are taken from Refs. [6,7], respectively. Furthermore, for the population distribution assumption $\rho_{11} \approx \rho_{33}$ we refer to Refs. [30,33].

ACKNOWLEDGMENTS

This work was supported by the National Natural Science Foundation of China (Grant No. 12174301), the Natural Science Basic Research Program of Shaanxi (Program No. 2023-JC-JQ-01), and the Fundamental Research Funds for the Central Universities.

[1] K.-J. Boller, A. Imamoğlu, and S. E. Harris, Phys. Rev. Lett. **66**, 2593 (1991).
[2] J. O. Weatherall and C. P. Search, Phys. Rev. A **78**, 053802 (2008).
[3] M. Fleischhauer, A. Imamoglu, and J. P. Marangos, Rev. Mod. Phys. **77**, 633 (2005).
[4] E. Paspalakis and P. Knight, J. Opt. B: Quantum Semiclassical Opt. **4**, S372 (2002).
[5] Z.-B. Wang, K.-P. Marzlin, and B. C. Sanders, Phys. Rev. Lett. **97**, 063901 (2006).
[6] A. MacRae, G. Campbell, and A. I. Lvovsky, Opt. Lett. **33**, 2659 (2008).
[7] H. M. M. Alotaibi and B. C. Sanders, Phys. Rev. A **89**, 021802(R) (2014).
[8] S. Li, X. Yang, X. Cao, C. Zhang, C. Xie, and H. Wang, Phys. Rev. Lett. **101**, 073602 (2008).
[9] H. M. M. Alotaibi and B. C. Sanders, Phys. Rev. A **94**, 053832 (2016).
[10] A. Joshi and M. Xiao, Phys. Rev. A **71**, 041801(R) (2005).
[11] M. Onoda, S. Murakami, and N. Nagaosa, Phys. Rev. Lett. **93**, 083901 (2004).
[12] K. Y. Bliokh and Y. P. Bliokh, Phys. Rev. Lett. **96**, 073903 (2006).
[13] M. Abbas, Ziauddin, and S. Qamar, Laser Phys. Lett. **11**, 015201 (2014).
[14] A. A. Khan, M. Abbas, Y.-L. Chaung, I. Ahmed, and Ziauddin, Phys. Rev. A **102**, 053718 (2020).
[15] M. Abbas, S. H. Asadpour, Ziauddin, P. Zhang, J. Ruseckas, and H. R. Hamedi, Phys. Rev. A **110**, 023730 (2024).
[16] M. Waseem, M. Irfan, and S. Qamar, Phys. Rev. A **110**, 033711 (2024).
[17] J. Sinova, S. O. Valenzuela, J. Wunderlich, C. H. Back, and T. Jungwirth, Rev. Mod. Phys. **87**, 1213 (2015).
[18] S. O. Valenzuela and M. Tinkham, Nature (London) **442**, 176 (2006).
[19] O. Hosten and P. Kwiat, Science **319**, 787 (2008).
[20] F. Cardano and L. Marrucci, Nature Photon. **9**, 776 (2015).
[21] K. Y. Bliokh, F. J. Rodríguez-Fortuño, F. Nori, and A. V. Zayats, Nat. Photon. **9**, 796 (2015).
[22] L. Cai, M. Liu, S. Chen, Y. Liu, W. Shu, H. Luo, and S. Wen, Phys. Rev. A **95**, 013809 (2017).
[23] S. Chen, X. Zhou, C. Mi, H. Luo, and S. Wen, Phys. Rev. A **91**, 062105 (2015).

[24] R.-G. Wan and M. S. Zubairy, Phys. Rev. A **101**, 033837 (2020).
[25] J. Wu, J. Zhang, S. Zhu, and G. S. Agarwal, Opt. Lett. **45**, 149 (2020).
[26] M. Waseem, M. Shah, and G. Xianlong, Phys. Rev. A **110**, 033104 (2024).
[27] M. Shah, S. Qamar, and M. Waseem, arXiv:2411.17256.
[28] L. Wu, H. S. Chu, W. S. Koh, and E. P. Li, Opt. Express **18**, 14395 (2010).
[29] Y. Xiang, X. Jiang, Q. You, J. Guo, and X. Dai, Photon. Res. **5**, 467 (2017).
[30] S. Rebić, D. Vitali, C. Ottaviani, P. Tombesi, M. Artoni, F. Cataliotti, and R. Corbalán, Phys. Rev. A **70**, 032317 (2004).
[31] A. S. Zibrov, M. D. Lukin, D. E. Nikonov, L. Hollberg, M. O. Scully, V. L. Velichansky, and H. G. Robinson, Phys. Rev. Lett. **75**, 1499 (1995).
[32] C. Y. Ye, A. S. Zibrov, Y. V. Rostovtsev, and M. O. Scully, Phys. Rev. A **65**, 043805 (2002).
[33] Y. Han, J. Xiao, Y. Liu, C. Zhang, H. Wang, M. Xiao, and K. Peng, Phys. Rev. A **77**, 023824 (2008).